AIAA-2025-3392

Control of Flow Circulations in a Programmable Offset Diffuser

Samuel Li[1], **Joshua W. Fletcher**[2], **Bojan Vukasinovic**[3], **James Mace**[4], **and Ari Glezer**[5]
Woodruff School of Mechanical Engineering, Georgia Institute of Technology,
Atlanta, GA, USA
Mory Mani[6]
Massachusetts Institute of Technology, Cambridge, MA, USA
Zachary T. Stratton[7] **and John T. Spyropoulos**[8]
Warfare Center – Aircraft Division, Patuxent River, MD, USA

A flow control approach to address total pressure distortions at the AIP of a reconfigurable diffuser testbed with variable bend section ($20° < \theta < 60°$) was developed and tested in a joint experimental/numerical study. The present investigation showed that distortion at the AIP is caused in large part by the presence of a pair of time-averaged counter-rotating streamwise vortices that evolve as a result of Dean circulations during flow turning in the bend. The circulation transports streamwise vorticity concentrations of opposite sense along the inner-radius surface about the bend's plane of symmetry that roll and are advected through a short diffuser to the AIP. The present flow control approach is designed to weaken or suppress the wall-bound formation of streamwise vorticity on the inner-radius surface of the bend using actuation by arrays of surface wall jets. Preliminary investigations of this fluidic control approach using fluidically-oscillating jets showed that it can successfully suppress and delay vorticity transport to the AIP by destructive interactions of jets-induced small-scale vorticity concentrations of opposite sense relative to the circulations-induced concentrations that pool along the bend surfaces. The effectiveness of the present configuration of fluidic actuation depends strongly on the Mach number and the bend angle, while the bend radius has only a secondary effect. Time-resolved analysis of flow demonstrated the impact of the actuation on the structure of the instantaneous flow and underscores the differences between the instantaneous and time-averaged flow fields.

---

[1] Graduate Research Assistant, AIAA Member
[2] Graduate Research Assistant, AIAA Member
[3] Senior Research Engineer, AIAA Member
[4] Consultant, AIAA Member
[5] Professor, AIAA Fellow
[6] Consultant, AIAA Member
[7] Aerospace Engineer, NAWCAD, AIAA Member
[8] Aerospace Engineer - Lead for Inlets, Nozzles, and Aeroacoustics, NAWCAD, AIAA Associate Fellow

Nomenclature

AFC = Active flow control
AIP = Aerodynamic interface plane
AR = Inlet/channel aspect ratio
C_q = Jet mass flow rate coefficient
D_{AIP} = AIP diameter
$DPCP_{avg}$ = Average circumferential distortion descriptor
$DPCP_h$ = Hub circumferential distortion descriptor
$DPCP_t$ = Tip circumferential distortion descriptor
$DPRP_h$ = Hub radial distortion descriptor
$DPRP_t$ = Tip radial distortion descriptor
L = throat-to-AIP length
r = Radius of curvature at the bend
r/D = Radius of curvature at the bend normalized by AIP diameter
M = Mach number
M_{AIP} = Mach number at the aerodynamic interface plane
TKE = Turbulent kinetic energy
θ = Bend turning angle
ω = Vorticity

I. Introduction

The development of next-generation military aircraft features streamlined propulsion/airframe integration and highlights the need for increasingly compact and complex engine inlet designs. These lower form factor inlets and diffusers allow for greater freedom of airframe design, stealth benefits, and potential drag and performance improvements. However, such compact and complex inlet apertures often include highly offset or serpentine-shaped diffusers and therefore pose significant challenges for managing their adverse internal flow characteristics. High-speed subsonic flows within offset diffusers are dominated by intense streamwise vortices, possible flow separation at moderate to high turning angles, or even a potential appearance of transonic shock. Without appropriate flow-management techniques, these secondary flow effects can cause significant total pressure losses, as well as distortion at the aerodynamic interface plane (AIP), leading to undesired aeromechanical interactions with the downstream compression fan blades and compromising turbomachinery performance.

Inlet concepts for future aircraft feature highly compact characteristic lengths in addition to aggressive centerline offsets with significant curvature exceeding existing design heritage. Connolly et al. [1] simulated the flow through a serpentine diffuser and found that the secondary flows were driven by a pair of counter-rotating Dean vortices [2]. Though Dean vortices have primarily been investigated in the context of laminar flow through bends, similar flow physics characterizes the flow within curved diffusers at higher duct-flow speeds. Dean [2, 3] analyzed flow through a curved pipe at low Reynolds numbers and found the flow is characterized by a pair of counterrotating streamwise vortices, nowadays known as Dean vortices, formed due the competing effects of the centrifugal force and pressure gradient. Towards the center of the bend, the fluid streamline is driven radially from the inner radius towards the outer radius due to the centrifugal force. However, viscosity near the surface of the upper and lower walls diminishes the effect of the centrifugal force, and the inward directed pressure gradient instead dominates. The Dean number was defined as: $De = Re\sqrt{D_h/R_c}$, where Re is the Reynolds number, D_h is the hydraulic diameter of the pipe, and R_c is the radius of curvature of the bend. This value quantifies this secondary flow phenomenon, its shape, and its general structure. More recently, numerical and experimental investigations have further validated these findings and expanded on the formation of these vortices. Dutta et al. [4] used a k-ε model and showed that though the vortices are initially formed near the outer perimeter of the duct, the curvature also induces a recirculation region that advects the vortices such that they coalesce at the inner bend of the duct. They also found that bend angle plays a significant role in the formation and structure of the streamwise vortices that are unaccounted for in the Dean number. Additionally, Winters [5] performed a numerical analysis of laminar flow through a rectangular bend and found that in the presence of strong enough pressure gradients, Dean vortices can split into a four-cell flow pattern, and by changing the aspect ratio of the bend, the formation of these four-cell flow patterns can further evolve. Sudo et al. [6] used hot wire anemometry to experimentally analyze turbulent flow through a square 90^o bend. They found that although the intensity of the secondary flows was maximum at the exit of the bend, the secondary flows continued to be relevant significantly downstream of the bend. Additionally, past the bend, the turbulent kinetic energy continued to grow, where it reached its maximum downstream of the bend exit. However, nearly all studies conducted on curved ducts have focused on low Reynolds number, incompressible flows. There is a demonstrated need to extend these investigations into the compressible regime of propulsion systems.

Over recent decades, passive and active flow control techniques have been developed and investigated to reduce the adverse effects of integrated inlet flow on propulsion system performance. Passive vortex generators have been used to improve recovery and reduce distortion by affecting the evolution of secondary flow vortices [7] and partially suppressing internal separation [8-10]. While these passive techniques have had varying successes, they can be undesirable compared to active flow control (AFC) as their drag effects lead to total pressure losses, and their passive nature means they lack the flexibility to adapt to changing flow conditions. To this end, many AFC approaches have been designed and tested. Scribben et al. [11] used microjets in a serpentine diffuser to reduce distortion by 70% and improve total pressure recovery by 2% at an AIP Mach number of 0.55 and jet mass flow rate coefficient C_q =0.01. Anderson et al. [12] numerically investigated a redesigned M2129 inlet s-duct and used optimized microjets to reduce DC60 distortion parameter below 0.1 with C_q =0.005. Gartner and Amitay [13] used pulsed jets, sweeping jets, and a blowing slot to improve total pressure recovery in a rectangular diffuser, and showed that the slot-jet was less effective than pulsed or sweeping jets. Rabe [14] evaluated microjets in a double-offset diffuser driven by a gas-turbine engine and, with the jets driven by bleed from the engine at a rate of 1%, was able to decrease circumferential distortion by 60% at M = 0.55. Harrison et al. [15] experimentally and numerically investigated a suction and blowing scheme for a thick boundary layer ingesting serpentine diffuser. At M = 0.85, they were able to reduce DC60 by 50% with a circumferential blowing scheme, but reduced DC60 by 75% by including suction. Garnier [16] performed spectral analysis comparing pulsed and continuous blowing in an aggressive s-duct using an array of dynamic pressure sensors, and concluded that the pulsed blowing could match the performance of continuous jets at half the C_q over $M = 0.2 – 0.4$. Amitay et al. [17] used an array of synthetic jets to completely reattach flow in a serpentine duct up to $M = 0.2$, while Mathis et al. [18] also used synthetic jets to reattach flow through an s-duct diffuser at $Re = 4.1x10^4$. Gissen et al. [19] used a hybrid approach of passive vanes and synthetic jets in a boundary layer ingesting offset diffuser to improve circumferential distortion by 35% at $M = 0.55$. Burrows et al. [20] utilized fluidic-oscillating jets to control the vorticity of a modified offset diffuser and reduced distortion by 68% with $C_q = 0.0025$ at $M = 0.55$. In an extension study, Burrows et al. [21] were able to mitigate the effect of local flow separation in a serpentine diffuser and decreased circumferential distortion by 60% with $C_q = 0.005$. Finally, Burrows et al. [22] added a cowl to the same serpentine geometry that produced strong inlet streamwise vortices and significant total pressure losses. These were mitigated using aerodynamic bleed through the cowl.

These prior efforts clearly showed that AFC technology can be successfully used to mitigate effects of adverse flow features with complex inlet designs. However, in earlier investigations, AFC has been incorporated into pre-existing fixed inlet designs as *a posteriori* approach for improving performance. This inherently precludes the investigation of the interaction of flow control actuation within the geometric and operational space during the design stage. The overarching objective of the present project is to demonstrate the effectiveness of incorporating AFC early in the design process. This was preceded by the development of a geometrically adaptive diffuser testbed that allows for rapid exploration of a range of inlet geometric design configurations as well as numerical simulation tools to allow for rapid variation of desired design characteristics [23]. The experimental testbed was designed and manufactured to allow rapid changes in the bend aspect ratio, angle, and its radius of curvature, as well as changes to the diffuser shape, section lengths, and other parameters. In addition, the setup enables easy integration of AFC at multiple points throughout the diffuser to mitigate the adverse flow effects within the flow path.

The present effort builds on the earlier work of Stratton et al. [23] and analyzes the sources of the flow distortion and losses that are associated with Dean circulations that originate in the diffuser's bend, followed by the development and demonstration of a fluidic actuation approach to counter the effects of these circulations. The test facility and diffuser design are presented in §II, the numerical setup and methodology are described in §III, and the underlying structure of the base flow, explored experimentally and numerically, is discussed in §IV. Finally, the present flow control approach and its implementation are described in §V using numerical simulations, and the experimental measurements of the effects of the actuation are analyzed in §VI, and the effects of the actuation on the flow physics are detailed further in §VII.

II. Experimental Setup and Flow Diagnostics

The present experiments are performed in the Georgia Tech open-return, pull-down, subsonic wind tunnel driven by a 150 hp blower, as shown schematically in Figure 1, along with the diffuser model. The steady-state total pressure distribution at the AIP is measured using a 40-probe total pressure rake within a cylindrical conduit having a diameter $D_{AIP} = 12.7$ cm. Downstream of the total pressure rake section, the flow is expanded through a tunnel diffuser and a 90-degree turn into the system's blower, controlled remotely by a variable frequency drive. The blower's outlet is connected to a flow silencer to reduce noise, and a water-cooled low-pressure drop heat exchanger (not shown) that is cooled by a dedicated chiller controls the return air within 1-2° C.

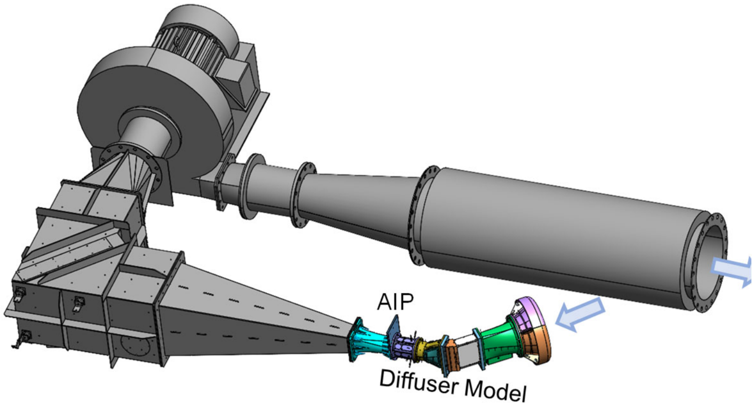

Figure 1. *CAD model of pull-down wind tunnel facility having the diffuser model at the intake.*

The programmable diffuser testbed (Figures 1 and 2), is constructed from interchangeable mating elements to yield independent variations of aspect ratio, bend turning angle, and turning radius. Ambient air is drawn through a bellmouth section having an inlet diameter $3.9D_{\mathrm{AIP}}$, followed by a circular to rectangular transition section to the inlet of a transparent constant cross-section channel upstream of an interchangeable bend section where bends of different angles and turning radii can be installed. The aspect ratio of the modular diffuser is set at $AR = 4$, while three bend inner radii $r/D = 0.2$, 0.35, 0.5 are tested, each with bend angles $\theta = 20°$, 40°, and 60° for a total of nine total bend geometries. A 3.8 cm long adaptor piece connects the bend to an expansion-contraction diffuser section that interfaces with the AIP. The diffuser is tested over a range of AIP Mach numbers $0.1 < M_{\mathrm{AIP}} < 0.6$, and it should be noted that while the model bends are in the horizontal plane, the experimental and numerical data are presented for bends in the vertical plane for convenience, as oriented in Figure 2.

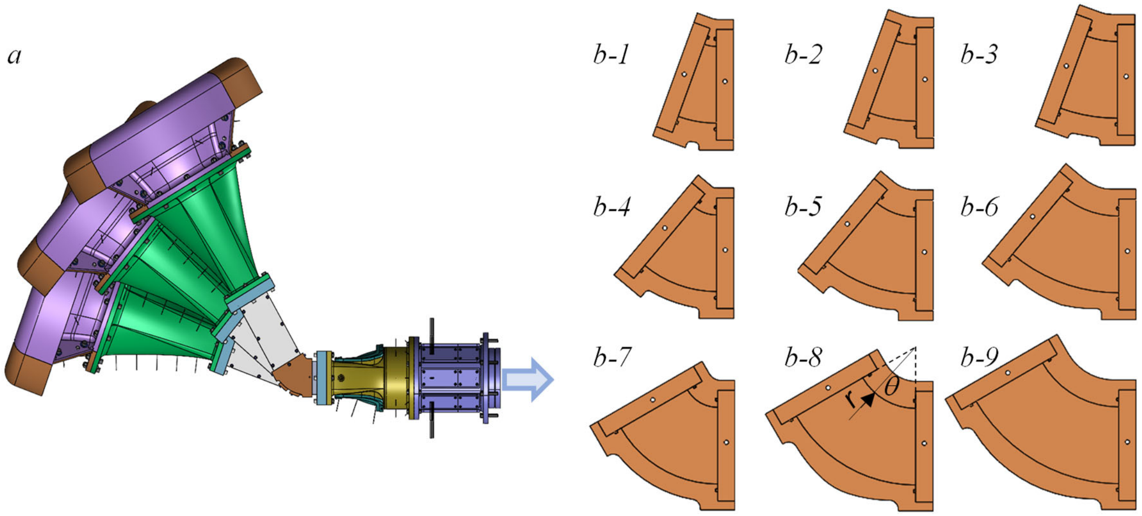

Figure 2. *Overlaid CAD of a modular diffuser model at $\theta = 20°$, 40°, and 60° bend angles (a) and all the bend variants of r/D =0.2 (b-1,4,7), 0.35 (b-2,5,8), and 0.5 (b-3,6,9), and $\theta = 20°$ (b-1–3), 40° (b-4–6), and 60° (b-7–9).*

A 40-probe total-pressure rake at the AIP is constructed from eight radial arrays, each of five total pressure tubes at $r/R = 0.27$, 0.38, 0.51, 0.67, and 0.9 that are azimuthally spaced 45° apart around the circumference of the AIP. The total pressure measurements are used to compute the total pressure recovery as well as the flow distortion descriptors per SAE ARP1420b [24]. The total pressure rake is supplemented with a matching array of eight static pressure ports that are each located on the diffuser wall 0.4*D* upstream of the AIP. Another azimuthal array of eight equally-spaced static pressure ports is located on the upstream end of the bellmouth. These bellmouth static pressure ports are used to calculate the Mach number and mass flow rate through the AIP using the calibration curve developed previously, utilizing the AIP total pressure rake and the ring of static pressure ports upstream of the AIP [23]. The mass flow rate is normalized with respect to standard sea level pressure and temperature conditions. Additional static pressure ports are distributed along the centerlines of the side and bottom walls of the bellmouth and diffuser sections, and the inner and outer surfaces of the bend. Static and total pressures are measured using a PSI Netscanner system, where each set of pressure measurements is averaged over 64 independent samples, while the time-averaged static and total pressures are computed from fifty such sets. The manufacturer specified accuracy of each scanner channel is ±17.25 Pa and the overall uncertainty of the time-averaged pressure is less than 1%, excluding possible localized uncertainty due to the local flow angularity. The static pressure around the circumference of the bellmouth is measured using a 10 torr MKS Baratron transducer (uncertainty of about 1.5 Pa) sampled using a computer-controlled rotary valve.

III. Numerical Setup

Flow Solver and Turbulence Model The charLES large-eddy simulation (LES) code, developed by Cascade Technologies (a subsidiary of Cadence Design Systems, Inc.), is used to solve the compressible, time-dependent, filtered Navier-Stokes equations for this diffuser and active flow control configuration. charLES utilizes a density-based finite-volume method on unstructured grids, where fluxes are computed with a second-order scheme [25]. The time integration uses an explicit third-order Runge-Kutta scheme. The mesh generation is handled by Stitch, a tool within the charLES suite, which is automatic and based on the computation of Voronoi diagrams [26]. This method results in a smooth mesh of nearly isotropic cells throughout the domain, which is well-suited for LES. To perform Wall Modeled large-eddy simulations (WMLES), charLES implements a wall-stress-based model to reduce the near-wall grid requirements based upon the algebraic formulation prescribed in the one-dimensional equilibrium stress model [27]. These equations are solved at each wall-adjacent cell centroid at each time step for wall shear stress, which serves as the Neumann boundary conditions for the momentum equations. This wall model does not account for the inner layer solution's unsteadiness or pressure gradient effects. The dynamic Smagorinsky model [28] is utilized to account for the sub-grid-scale stresses.

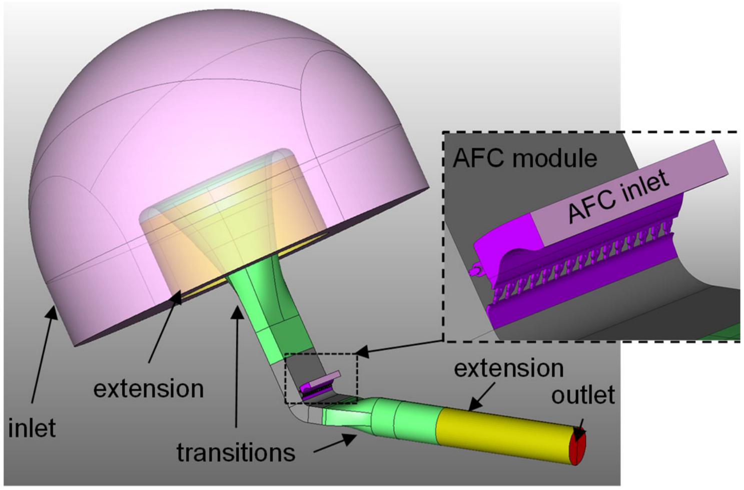

Figure 3. *Computational domain.*

Computational Domain and Simulation Details The computational domain used for the diffuser in this study is shown in Figure 3 and is based on the CAD model of the Georgia Tech facility and test model hardware. The AFC module is installed upstream of the bend, shown in purple. In the baseline case, this module is removed and replaced with a simple flat wall. The bellmouth is extended (shown in yellow) to incorporate a sizeable hemispherical inlet region. A total pressure boundary condition is applied to the hemispherical inflow surface, set at standard atmospheric day conditions. A mass flow boundary condition is applied to the AFC plenum inflow surface, such that an exact C_q is specified. The tunnel walls are set as no-slip walls where the algebraic equilibrium wall model is applied. The extensions, downstream of the AIP, are set as free-slip walls. The outlet is a pressure boundary condition, where the pressure is set to achieve a desired mass flow rate at the AIP. To date, simulations were conducted at $M_{\mathrm{AIP}} = 0.4$ at $\theta = 60^{\circ}$ and $r/D = 0.2$ without AFC (i.e. baseline) and with AFC on at $C_{\mathrm{q}} = 0.01$. Additionally, three separate simulations were completed at $M_{\mathrm{AIP}} = 0.4$ for an AFC testbed configuration, which utilizes periodic boundary conditions to isolate the fluidic oscillators; this will be discussed in §V.

The grids used in this study are based on the findings from the AFC testbed configuration (§V) and the grid sensitivity study for the baseline tunnel. Details of the meshes and validation can be found in Stratton et al. [23]. The total number of elements in the computational domain is 250M and 380M for the baseline and AFC configurations, respectively. The average y^{+}, measured at the gray walls in Figure 3, is 24 and 28 for the baseline and AFC configurations, respectively. All simulations were run on the U.S. Department of Defense Narwhal and Wheat clusters using GPU resources. Using 40 NVIDIA A100 GPUs, the simulation completes 40 characteristic diffuser-flow-convection times in 24 hours, utilizing the distance between the throat and AIP.

IV. Characterization of the Base Flow

Although the present diffuser configuration excludes the rectangular section downstream of the bend that was used by Stratton et al. [23], the topology of the base flow at the AIP in the absence of this section is similar. Figure 4 shows the time-averaged total pressure distributions in the experimental setup for each of the nine variants of the bend geometry (cf. Figure 2b) at $M_{\mathrm{AIP}} = 0.4$. The total pressure distributions exhibit two domains of total pressure deficit at the top and bottom of the AIP that are associated with the flow over the convex (inner) and concave (outer) surfaces of the bend, whereas the dominant deficit is associated with the convex side of the surface of the bend. While the similar flow topology in all realizations shown in Figure 4 suggests similar underlying flow physics, there are some secondary modifications of the flow/total pressure topology with changes in the bend angle and radius. The total pressure signature at the AIP, which is aligned with the inner bend surface (at the top), indicates that the most pronounced pressure deficit is for the highest bend angle and the lowest radius (Figure 4g). In general, as the bend angle increases, there is both the radial

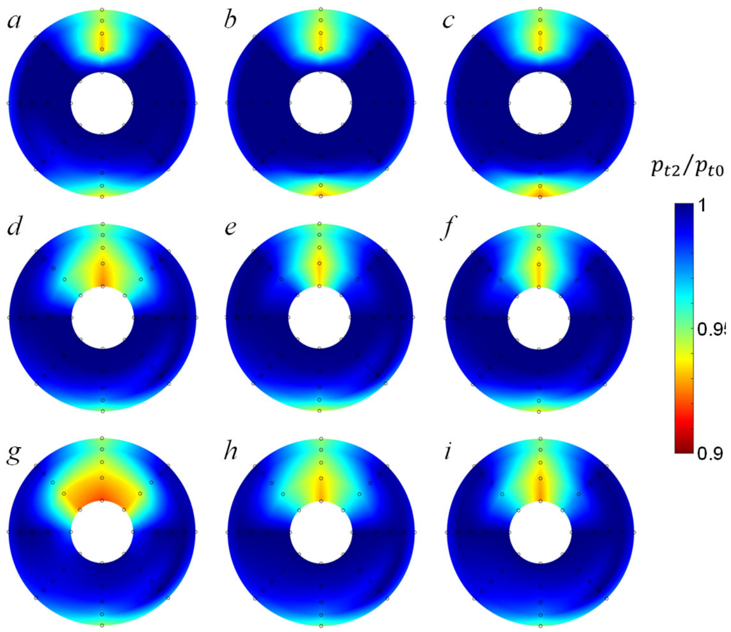

Figure 4. *Color raster plots of the total pressure at the AIP at* $M_{AIP} = 0.4$ *for r/D =0.2 (a,d,g), 0.35 (b,e,h), and 0.5 (c,f,i), and* θ = 20° *(a,b,c),* 40° *(d,e,f), and* 60° *(g,h,i).*

and azimuthal spread of the deficit domain, although it subsides with the increase in the bend radius (e.g., compare the change between Figures 4a and g, and Figures 4c and i). It is important to note that in all configurations besides $\theta = 20°$, the deficit spreads into the core flow beyond the outermost top total pressure rake. When comparing the deficit domain change with the bend radius, the lowest bend angle cases (Figures 4a–c) also stand out relative to the others. The deficit domain progressively shrinks with the increase in the bend radius for the two highest θ, while there is relatively little change for $\theta = 20°$. The AIP signature of the flow over the outer bend (at the bottom) indicates a rather weak and confined deficit region of the total pressure deficit. Although still weak, it is interesting that the highest deficit at the bottom is measured for the lowest bend angle (Figures 4a–c), and that it further diminishes with the increase in θ. Although very subtle, there is also a slight increase in the total pressure deficit at the bottom AIP region with the increase in the bend radius. Nonetheless, these measurements indicate that the primary source of the total pressure deficit and distortion is localized at the top region of the AIP, suggesting that the source of the flow associated with this AIP is tied to the flow over the inner bend. Consequently, this also identifies the region along the configuration that can be strategically targeted by flow control to mitigate the AIP total pressure distortion.

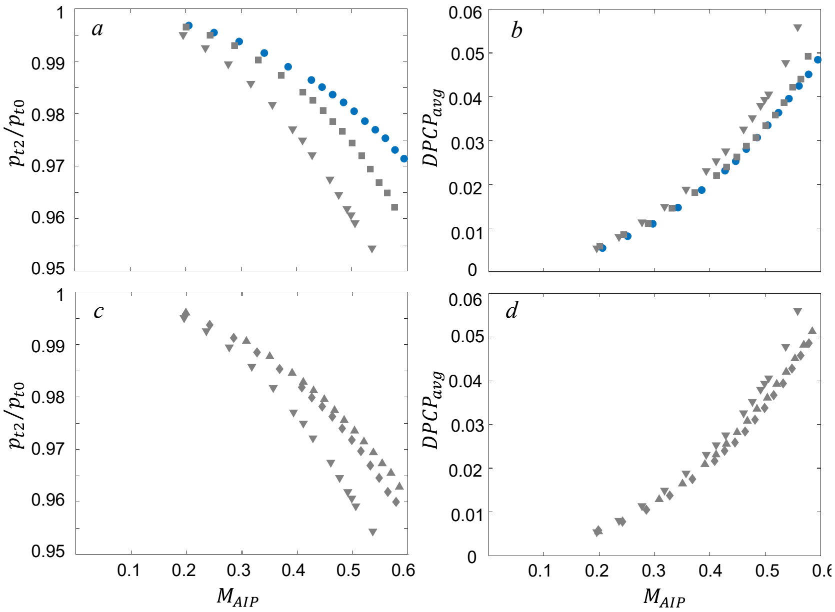

Figure 5. *Pressure recovery (a, c) and* $DPCP_{avg}$ *(b, d) for θ=20°(●), 40°(■),60°(▼) at r/D = 0.2 (a, b), and for r/D=0.2(▼), 0.35(♦), 0.5(▲), at θ=60°(c, d). Gray symbols reference instances where the total pressure deficit extends beyond the 40-probe rake inner array.*

To quantify the total pressure field at the AIP for the varying bend angles and radii, Figure 5 shows the measured evolution of the time-averaged total pressure recovery and distortion for the fixed radius $r/D = 0.2$ and each of the bend angles $\theta = 20°$, 40°, and 60°, over a full range of the Mach numbers $0.2 < M_{\mathrm{AIP}} < 0.6$ (Figures 5a,b) and for the fixed bend angle $\theta = 60°$, across all three radii $r/D = 0.2$, 0.35, and 0.5, and the full sweep of Mach numbers (Figures 5c,d). To emphasize when the total pressure deficit domain spreads outside of the 40-probe rake (as already discussed in connection with Figure 4), such data points are shown in gray instead of their default color assignment. Pressure recovery distributions in both Figures 5a and c depict a drop in recovery with increasing Mach number, leading to the maximum loss in total pressure between 3 – 4.5 % at the highest tested Mach numbers. Recovery decreases with the rate that strongly depends on the bend angle (Figure 5a), while increasing with larger bend radius, as seen in Figure 5c. It is interesting that a weaker dependence of the 5-ring average of the circumferential distortion parameter $DPCP_{\mathrm{avg}}$ is seen in either case (Figures 5b and d). In all the cases, there is a sharp rise in the distortion parameter with M_{AIP}, even exceeding $DPCP_{\mathrm{avg}} = 0.05$ at the highest Mach numbers. There is virtually no difference between the distortion levels for $\theta = 20°$ and 40° (Figure 5b), although it should be noted that the former is the only case where the full spatial-extent of the total pressure field is captured by the 40-probe rake. Once the bend angle is increased to $\theta = 60°$, there is some increase in the distortion parameter relative to the other two angles, as expected. Still, all the flow topologies for $\theta = 60°$ at the AIP indicate that the total pressure deficit extends beyond the 40-probe rakes. A rather similar variation with the bend radius is seen in Figure 5d. While it would be expected that distortion generally increases with the decrease in the bend radius, which leads to local flow separation, some increase is seen for the smallest radius $r/D = 0.2$, while the other two radii have nearly identical $DPCP_{\text{avg}}$ values.

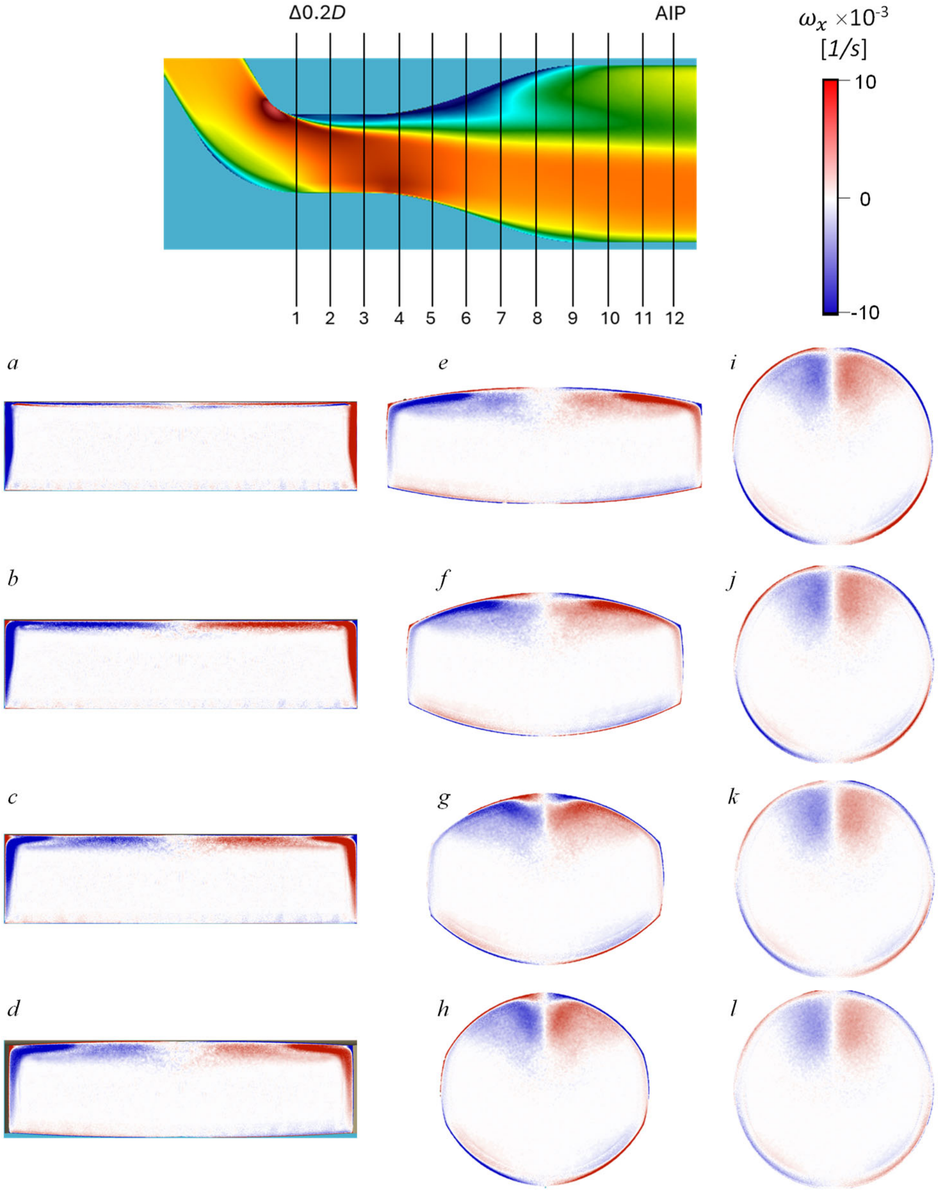

Figure 6. *Color raster plots of the time averaged streamwise vorticity (a – l) across 12 equally spaced cross sections 1 – 12 downstream of bend at* $M_{AIP} = 0.4$, *r/D = 0.2, and* $\theta = 60°$.

The next step for the flow control approach selection is related to the sources of the distortion that are analyzed in Figures 4 and 5. Since a previous comparison between the experimental investigations and numerical WMLES in a similar geometry [23] indicated a high fidelity of numerical simulations, a better insight into the source(s) of the baseline flow distortion is attained by analyzing the vortical flow evolution through the flow geometry of numerical simulations. Figure 6 illustrates the base flow mean vorticity evolution at $M_{\text{AIP}} = 0.4$ past the bend ($\theta = 60°$ and $r/D = 0.2$) and into the AIP. This is shown in twelve equidistant planes having $\Delta x/D = 0.2$. The two important features of the flow are noted at the exit plane of the bend (Figure 6a). Thick vorticity layers are seen already formed along the side walls, mirrored about the central plane. Simultaneously, thinner vorticity layers are seen along the inner-bend / top surface. It is argued that the thickened vorticity layers on the side walls are artifacts of the bending of incoming vorticity lines into the bend, coupled to the Dean circulation. At the bend entrance, vorticity lines are aligned across the boundary layers' span, i.e., parallel to each wall. Kinematically, the outer/bottom line advances farther than the inner/top line through the bend, inducing the tilt of the side vortical lines. Such a tilt gives rise to the streamwise component of vorticity, which has a counterclockwise (CCW) sense on the right-side wall in Figure 6a, and clockwise (CW) sense on the left-side wall. Another interesting feature is seen along the bottom surface, where a weak but detectable array of vortical concentrations is noted. These are consistent with the development of Görtler vortices [29] that form due to the flow instability of boundary layer flows over concave surfaces, such as the outer bend surface. In the next several downstream planes (Figures 6b–d), a rather swift sweep of the side vorticity layers is seen up and along the surface, accumulating the CCW and CW vorticity concentrations along the inner-bend surface. Such a swift convection of vorticity can be attributed to the Dean circulation in bends [2,3], the sense of which aligns with the vorticity transfer in this flow configuration. It is also noted that, as the two vorticity layers approach each other about the central plane of the channel, the vorticity signature in that region becomes spread and diffused progressively from Figure 6b to Figure 6d, arguably due to their interactions. Once the flow geometry begins to transition from rectangular to circular at the AIP, adverse pressure gradient along the inner-bend (top) side further assists in thickening of these layers (Figures 6e, f) and begin to roll into two central vortical structures (Figures 6f, g). A coherent sense of rolling is supported by the emergence of the secondary senses of vorticity underneath the primary vortical structures. These secondary vortical structures (Figures 6g, h) are typically spawned off the wall vorticity layer due to the presence of coherent vortical motions in the wall proximity, which is consistent with the vortical composition seen at these cross sections. Interestingly, once the flow geometry transitions to circular (Figures 6i–l), only the counter-rotating vortex pair remains dominant in the mean flow. Besides the boundary layer vorticity seen along the circumference, there is only an additional weak compressed vorticity layer along the opposite side, i.e., the side that corresponds to the outer bend surface, which initially indicated the presence of Görtler vortices [29]. At the AIP, the counter rotating structures formed on the inner bend by the Dean circulations show a high degree of correlation with the observed pressure distortion signature, a result of the vortices advecting low momentum fluid from the boundary layer into the core flow.

V. Flow Control Approach

As seen in the numerical results, the streamwise evolution of the time-averaged concentrations of streamwise vorticity of opposite sense (Figure 6), which leads to the presence of a counter-rotating vortex pair at the AIP, identifies the vorticity layers along the side walls of the bend as the main sources of their vorticity that is advected by the streamwise flow and transported by the Dean circulations. The present flow control approach to affect the evolution of these vortices and thereby mitigate the induced distortion at the AIP focuses on the transport and pooling of the streamwise vorticity along the side walls and over the inner bend surface as discussed in connection with Figure 6. Flow actuation is devised using surface jets across the inner surfaces of the bend to counter transport and pooling of the concentrations of streamwise vorticity that are induced by the counter-rotating Dean circulations across the bend. A spanwise array of wall jets was integrated using a module placed immediately upstream of the bend, as shown in Figure 7a. This arrangement enables easy variations of the bend geometry while using a single flow control module. The actuation wall jets are formed by fluidically oscillating jets similar to the actuators that were used in earlier investigations of offset and serpentine diffusers (e.g., [30, 31]). As shown in Figure 7b, the jets are fanned outward from the center plane, such that they induce a prevailing sense of vorticity opposing that present in the baseline flow across the side of the span they act on. It is expected that their interaction with the pooling flow over the upper side surface (past the bend) will be destructive and, at a minimum, induce a delay in the formation of the dominant vortical structures. Prior to the application of the designed and manufactured flow control arrays, a representative array, having all the jets issuing normal into still air, is tested on a bench, primarily with respect to the individual jet uniformity. The velocity distribution is measured along the downstream edge of the flow control module, i.e., along the interface with the bend, when installed in the model. The full spanwise measurement is shown in Figure 7c, where the jet array is overlaid along the horizontal axis for reference. The measurements indicate a reasonable uniform velocity (periodic) distribution, with a peak variation of ±4.1% of the mean. In addition, detailed measurements of such velocity profiles are conducted across three neighboring jets and for three jets' flow rates. When these profiles are scaled by the peak velocity and distance to the peak s-$s_{\max}$ relative to the distribution half-width w, they all collapse on the same velocity distribution, as shown in Figure 7d.

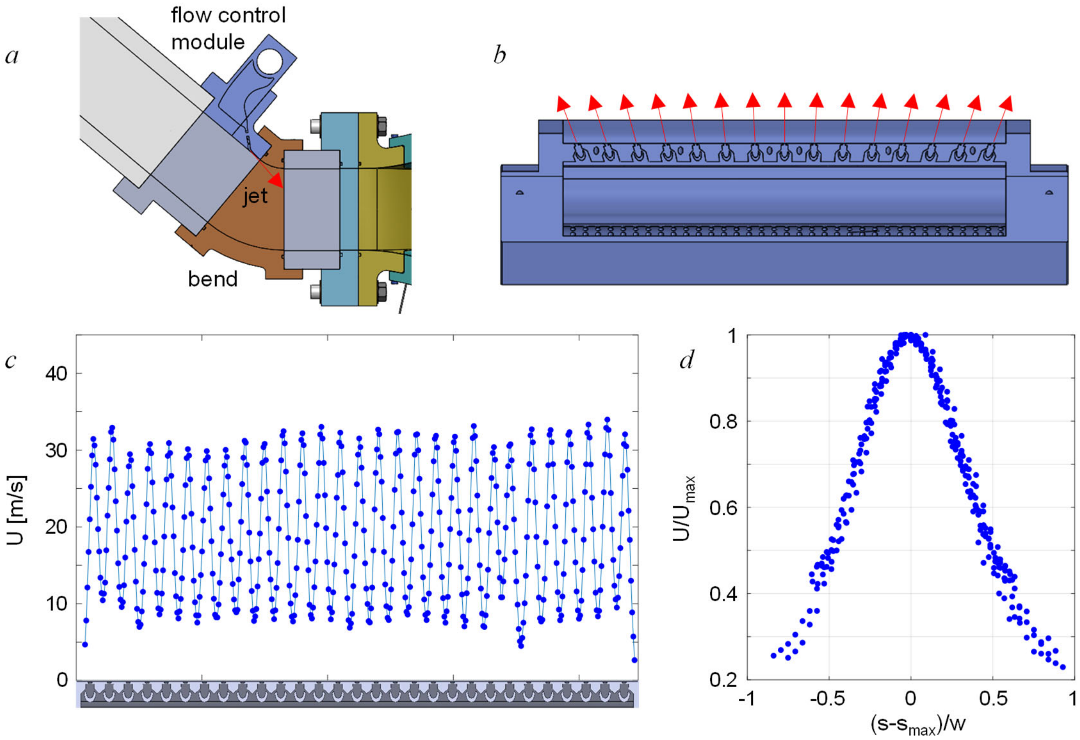

Figure 7. *Schematics of the slow control module integrated upstream from the bend (a) and its cross-section showing fifteen control jets (b). Bench-test calibration of the jets' linear array showing the jets' velocities across the full array (c) and the overlaid profiles of the 3 neighboring jets (d).*

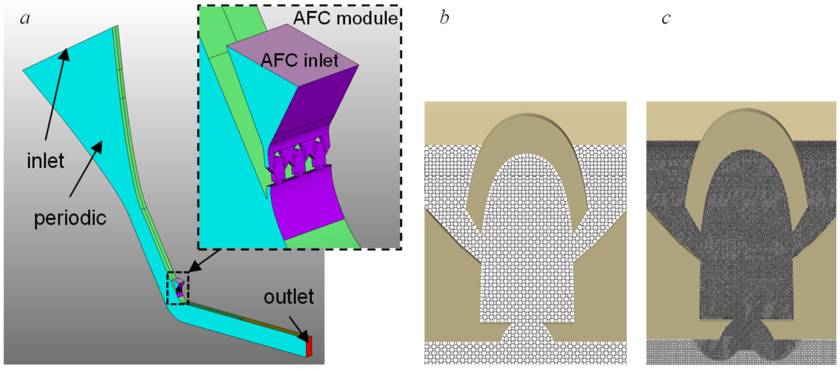

Figure 8. *Simplified AFC computational domain (a) M1 grid resolution (b) M2 grid resolution (c).*

Numerically, to assess computational costs, setup, and flow behavior over a range of AFC flow rates, a simplified AFC domain was constructed initially, as shown in Figure 8a. This domain focuses only on integration of the flow control elements used in experiments, and maintains the duct height and sizing of the full domain, shown in Figure 3, but excludes the AIP transition and applies periodic boundary conditions on the sides, such that only 3 fluidic oscillators are simulated. The Mach number in the constant area section of the duct is maintained at M_{AIP} = 0.4 and C_q = 0.005, 0.01, and 0.015 were evaluated. In addition, two mesh resolutions were evaluated, where Figure 8b is representative of the finest cell size present in the baseline duct study [23], while the mesh size shown in Figure 8c reduces the isotropic cell length by a factor of four within the actuator body and just outside of the exit.

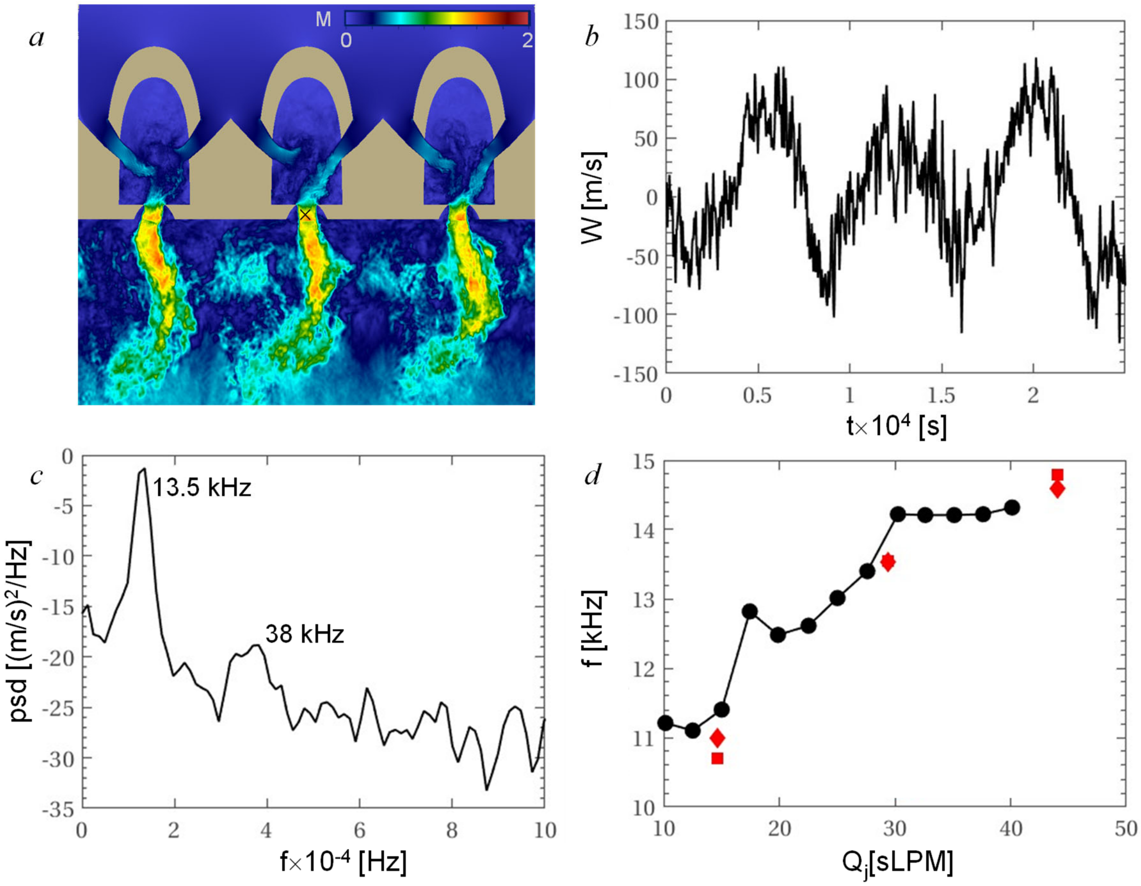

Figure 9. *Mach number contour for C_q = 0.01 (a), z-velocity signal at probe location for C_q = 0.01 (b), Power spectral density for C_q = 0.01 (c), sweeping frequency as a function of jet flow rate (d): WMLES-M1 (♦), WMLES-M2 (■), and Burrows et al. [30] (●).*

The results for $C_q = 0.01$ and the mesh M2 are shown in Figures 9a–c. Figure 9a is an instantaneous color raster plot of Mach number across the central horizontal plane of the fluidic actuator body. Although just a snapshot, this field still indicates the unsteady nature of the actuator operation. Inside the body, shear layers off the flow entries into the body point to the flow being passed through the right leg (in this view) to the orifice, while the shear layer bending towards the actuator base on the opposite side illustrates a moment of dominance of one side of the inflow. During the periodic operation, under the self-induced instability of the two colliding shear layers, this dominance switches between the two streams, representing the 'inner' flow oscillation. It is interesting to note that, while the three actuators appear close in phase, they are not locked and, in principle, do not operate phase-locked naturally. Besides the inner flow unsteadiness, switching of these two streams into the jet orifice results in the oscillating or 'sweeping' resulting jet behavior, which exhibits both temporal and spatial oscillation, along with the growth away from the orifice, as seen in the lower half of the flow depicted in Figure 9a. It is noted that at $C_q = 0.01$, there are shocks present in the jet being issued out of the orifice, having the peak Mach numbers around 2. A numerical 'probe' was placed just downstream of the sweeping fluidic oscillator jet, and the corresponding sampled signal of the z-component of velocity is shown in Figure 9b. Clearly, there is a dominant oscillation frequency of the velocity, which, due to the probe positioning, represents twice the frequency of the jet oscillation (from the left-to-right-most excursions). Figure 9c illustrates spectral content of such oscillations, based on the power spectral density of velocity fluctuations, indicating a peak frequency of about 13.5 kHz, which suggests that the jets oscillate at about 6.75 kHz at the prescribed $C_q = 0.01$. In addition, multiple broader frequency bands are seen in the signal, albeit with much lower contributions. The next higher is labeled on the plot at about 40 kHz, which is fairly close to the second harmonic of the dominant frequency, but it also appears to be related to the shear layer shedding frequency at the lip of the fluidic oscillator. Lastly, Figure 9d plots the sampled signal frequency from the present WMLES simulations against the prior experimental bench test data. As known, the frequency of oscillation increases with the flow rate through the fluidic oscillator, which is confirmed in both the experiments and simulations. Additionally, it is shown that the mesh resolution within the fluidic oscillator has only secondary impact on determining the sweeping motion or frequency; hence, the M1 resolution is used in the study of the full duct and AFC array shown in Figure 3.

VI. Flow Control Effects

The experimentally measured effects of the actuation are illustrated in Figure 10 at $C_q = 0.01$ using distributions of the time-averaged total pressure at the AIP for each of the nine bend configurations discussed in connection with Figure 4. These data show that in all configurations, the actuation causes a general flattening of the region of total pressure deficit, forcing advection of low momentum fluid to the upper surface at the AIP. At the lowest bend angle $\theta = 20°$ (Figures 10a– c), flow control at that prescribed level successfully mitigates nearly all the pressure distortion observed at the AIP associated with the inner bend side. Clearly, no effect is seen on the opposite, outer-bend side at the AIP, as the flow control effects along the upper surface do not couple with the flow over the outer bend. While the control at higher bend angles shows the same qualitative effect, the residual deficit increases with θ, implying that a higher C_q might be needed for higher θs, essentially rendering C_q as not the universal parameter. However, since the flow control axial location is fixed, its relative distance to the bend exit plane changes with θ, and it can also be argued that C_q might be preserved with adjustment of the location of the jet array issuance. Only minor variation of the AIP total pressure topology is seen when the bend radius is varied for any fixed θ. While the discrepancy increases for higher bend angles, the flow control efficacy seems to be only weakly dependent on the tested bend radii across all the cases.

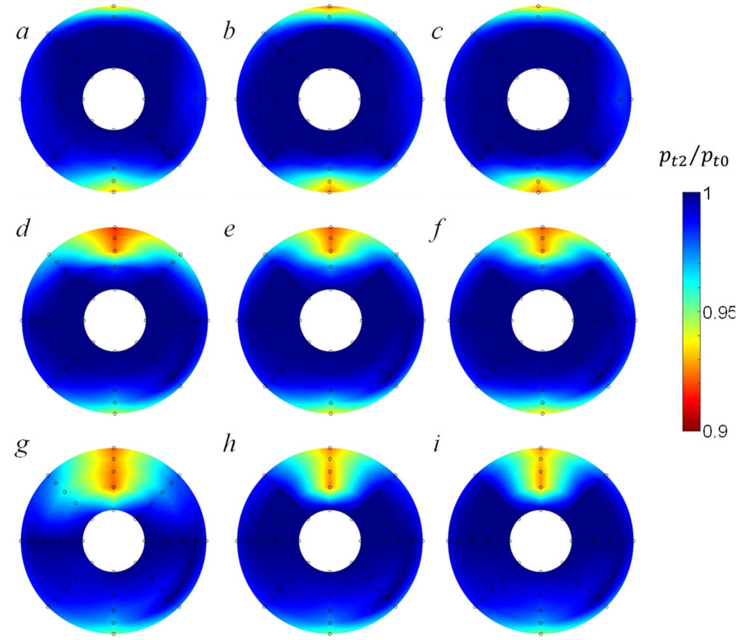

Figure 10. *Color raster plots of the total pressure at the AIP at* $M_{AIP} = 0.4$ *utilizing AFC at* $C_q = 0.01$ *for r/D =0.2 (a,d,g), 0.35 (b,e,h), and 0.5 (c,f,i), and θ = 20° (a,b,c), 40° (d,e,f), and 60° (g,h,i).*

It is informative to assess how the AIP distortion progressively changes as the flow control coefficient is increased. This is illustrated in Figure 11 for the $r/D = 0.2$ and $\theta = 40°$ case at $M_{\mathrm{AIP}} = 0.4$. The base flow (also previously shown in Figure 4d) shows a significant penetration of the low-pressure region into the core flow. While not capturing the full extent of the total pressure deficit, the 40-probe-measured circumferential distortion descriptor $DPCP_{\mathrm{avg}} = 0.0225$ for this flow. As the flow control parameter C_{q} is initially increased from zero, it is seen that the distortion descriptor does not change up to about $C_{\mathrm{q}} = 0.003$. It is not uncommon for the flow control effect to be delayed until a critical level of the flow control parameter is reached. However, in this case the analysis is further complicated by the total pressure deficit initial spread into the core flow. In fact, once the flow control clearly pushes the deficit domain away from the core flow and into the annular domain that is covered by the 40-probe rake, distortion parameter indicates an initial increase from the base level, up to $DPCP_{avg} = 0.0248$ for $C_{\mathrm{q}} = 0.005$. With the further increase in C_{q}, the deficit domain continues to be compressed against the top surface and begins to spread azimuthally outward, as seen for $C_{\mathrm{q}} = 0.008$. A notable drop in the distortion parameter is only seen in the upper range of the tested flow control parameters, falling to $DPCP_{avg} = 0.0188$ for $C_{\mathrm{q}} = 0.01$. Although not shown, spot checks with C_{q}s higher than 0.01 indicate a continuation of this trend in reducing the distortion descriptor with a further increase in C_{q}.

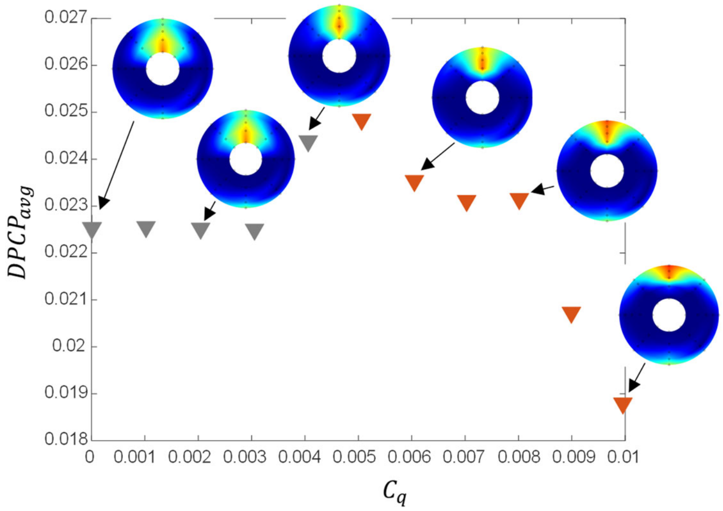

Figure 11. *Variation of the total pressure distortion* $DPCP_{avg}$ *with flow control parameter* C_q *at* $M_{AIP} = 0.4$*, r/D = 0.2, and* $\theta = 40°$*. Raster color plots of the corresponding AIP total pressure distributions are overlaid for reference.*

A more comprehensive analysis of time-averaged AIP recovery and distortion parameters for the $r/D = 0.2$ and $\theta = 40°$ case, measured across a full spectrum of Mach numbers and flow control parameters, is presented in Figure 12. As per the SAE specification ARP1420b [24], besides the circumferential distortion parameter averaged across the AIP face that was already discussed, $DPCP_{avg}$ (based on five azimuthal rings of eight probes each), the circumferential distortion ($DPCP$) and radial distortion ($DPRP$) descriptors are also used across the two innermost and two outermost rings, relevant for the hub and tip of the compressor blades, and are denoted with the h and t subscript respectively. By isolating the effects of the hub and tip parameters, the relative impact of the total pressure distortion and subsequent suppression due to the active flow control on the downstream turbomachinery can be asserted.

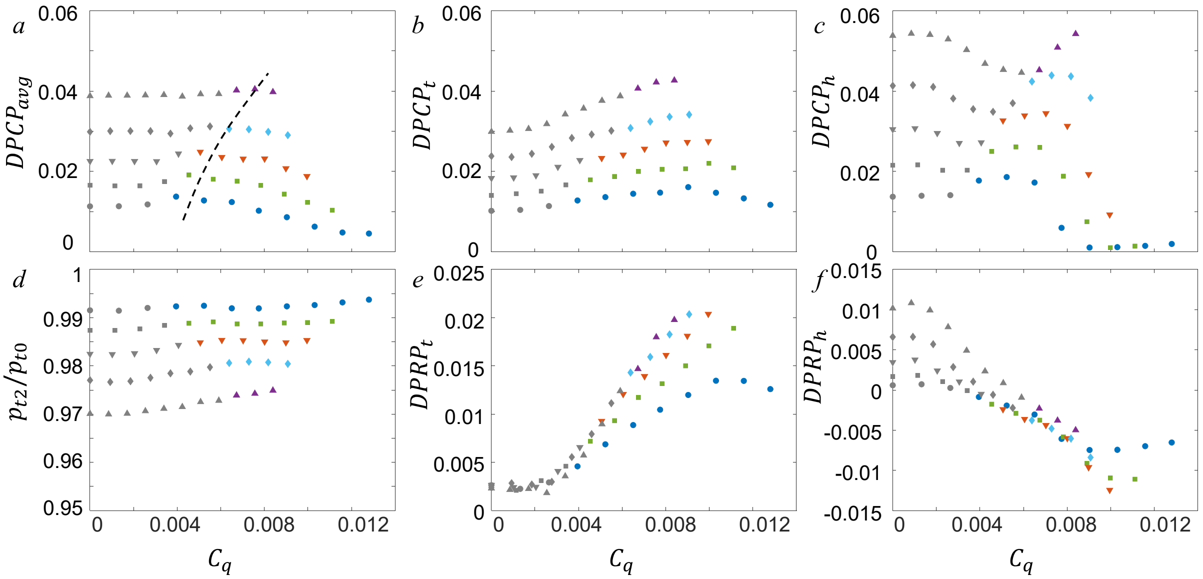

Figure 12. *Variation of the recovery* p_{t2}/p_{t0} *(d) and distortion Parameters* $DPCP_{avg}$ *(a),* $DPCP_t$ *(b),* $DPCP_h$ *(c),* $DPRP_t$ *(e), and* $DPRP_h$ *(f) with r/D = 0.2, θ =40° bend and* M_{AIP} *=0.3 (●), 0.35 (■), 0.4 (▼), 0.45 (◆), 0.5 (▲). Gray symbols reference instances where the total pressure deficit extends beyond the 40-probe rake inner array.*

Figure 12a shows the flow control effect on $DPCP_{avg}$ across the full range of Mach numbers $0.3 < M_{AIP} < 0.5$. While the distortion parameter is by definition based on the 40-probe rake, symbols in gray indicate that the total pressure deficit at the AIP extends beyond the innermost rake ring, just as a reference. It is noted that the typical full response to the flow control is seen only at $M_{AIP} = 0.3$, where the initial unchanged distortion is followed by a reduction proportional to C_q, which eventually subsides in an asymptotic manner. It is also noted that the highest flow control C_q is attained for the lowest Mach number flow – an artifact of the limited dimensional flow rate supplied to the control jet array. Nonetheless, a similar trend is seen for different Mach numbers, with the onset of effectiveness shifting to higher C_qs with the increase in M_{AIP}, which is emphasized by the dashed line in Figure 12a.

Figures 12b and e suggest that both the circumferential and radial distortions at the tip follow an inverted parabolic trend with C_q for all Mach numbers, with the distortion first increasing before beginning to decrease. While $DPCP_t$ appears to scale linearly with higher Mach numbers, its radial counterpart, $DPRP_t$, shows a tendency for the effect of higher Mach numbers to be diminished at any given C_q. The localized distortion behavior at the hub is noticeably different. $DPCP_h$ (Figure 12c) is shown to vary slightly before sharply decreasing with higher values of C_q, and eventually becoming fully attenuated at a sufficiently high C_q. This is compared to $DPRP_h$ (Figure 12f) which exhibits a near linear decrease with C_q before tapering off. Overall, across the range of C_qs tested in this investigation, tip distortion is expected to increase while hub distortion drastically decreases. This aligns with the qualitative observation of the region of low total pressure being shifted towards the outer ring of the AIP at increasing levels of flow control. The overall reduction in hub distortion at the AIP is of particular relevance to downstream compressor aeromechanics as discussed by Bloch et al. [32]. Distortion patterns imposed at the hub of the fan are deemed to be more critical in nature as irregularities will be transmitted directly into the core flow where they may be further destabilized by regions of temperature variance. This is in contrast to distortion patterns on the tip region, where spatial variations of pressure will travel down the bypass duct and are of less impact to engine flow instabilities of modern fans. Thus, despite the apparent increase in tip distortion induced by moderate levels of AFC actuation, an improvement in downstream engine instabilities is expected due to the reduction in both circumferential and radial hub distortion.

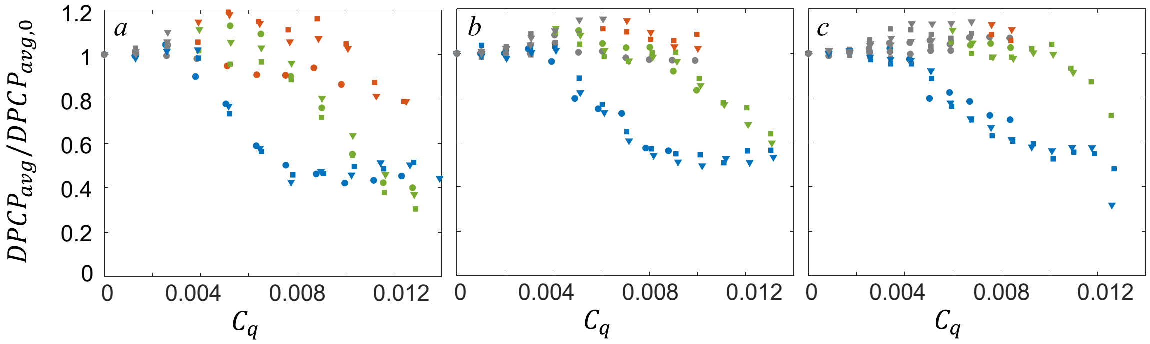

Figure 13. *Normalized DPCP$_{avg}$ at M$_{AIP}$ = 0.3 (a), 0.4 (b), 0.5 (c) for r/D = 0.2 (circle), 0.35(square), 0.5(triangle) and θ =20°(blue), 40°(green), 60°(red).*

The results for the primary distortion parameter $DPCP_{avg}$ for all nine geometrical variants of the bend are further considered in Figure 13, where all the controlled-flow results are normalized by the corresponding baseline flow distortion, $DPCP_{avg,0}$ (at C_q = 0). At any given degree of actuation, expressed by C_q, the reduction in AIP distortion parameter is primarily governed by bend angle θ, with the radius of curvature having only a secondary effect. As intuitively expected, bends of lower turns experience the greatest percentage reduction in distortion due to flow control, and the effect progressively subsides with the increase in θ. For θ = 20°, the region of low total pressure at the AIP is nearly fully suppressed at higher levels of C_q, leading to maximum decrease in distortion by about 50% for all bend radii. Up to $M_{AIP} = 0.4$ (Figure 13b), the flows in bends of θ = 40° can achieve the same degree of reduction in $DPCP_{avg}$ as bends of θ = 20°. At greater bend angles, there is also generally higher variance in the effects of different bend radii. This data suggests that the optimal geometric configuration for bends in serpentine inlets with built in flow control will depend on available C_q, although significant improvements can generally be expected near the levels of $C_q \approx 0.01$. Also, it is expected that optimization of the flow control axial location and possible integration in the bend will yield further improvements in the flow control effectiveness or conversely, required C_q for a prescribed effect to be reduced. In addition, when the overall *L*/*D* of the intake is a priority, bend radius can be decreased at less cost to overall distortion than increasing the bend angle.

VII. The Evolution of the Controlled Flow

Further analysis of the simulated controlled and uncontrolled flow fields is undertaken with the

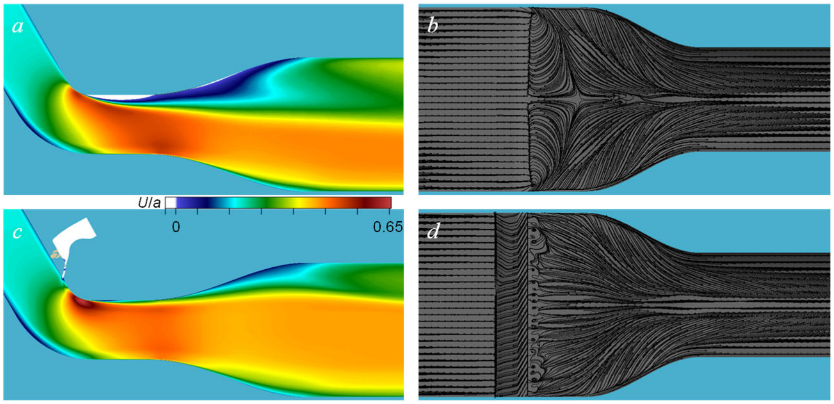

Figure 14. *Average Mach number contour along the duct centerline for baseline (a) and AFC (c) and near-surface streamlines along the top surface for baseline (a) and AFC (d) for* $M_{AIP} = 0.4$, *r/D = 0.2, and* $\theta = 60°$.

objective of assessing the intended active flow control effect on the vortical flow evolution into the AIP. The contour of the streamwise velocity non-dimensionalized by the speed of sound along the centerline for the baseline and $C_q = 0.01$ case for $M_{AIP} = 0.4$, $\theta = 60°$ and $r/D = 0.2$, are shown in Figures 14a and c, respectively, while the corresponding near-surface streamlines are shown in Figures 14b and d. In the baseline flow (Figures 14a and b), the flow topology on the inner bend side indicates a typical dual-cell separation domain, symmetric about the centerline, that has a sharp onset across the full span and gradual reattachment, from the sides toward the central plane. Past the reattachment, the central flow sharply converges into the core upstream of the AIP, while the outer traces indicate more folding of the flow inward. While the reversed flow topology occupies a sizable spanwise domain (Figure 14b), velocity distributions in Figure 14a clearly indicate that it is also very shallow, i.e., that its main effect on the base AIP flow is likely reflected not by the locally separated flow but by a significant velocity/momentum/total pressure deficit of the reattached flow, as marked by the blue-colored domain in Figure 14a. Clearly, this deficit becomes only amplified along the diffusing side of the geometry transition into the AIP round section. In the presence of flow control, traces of the jets become clearly visible upstream of the baseline flow separation (Figure 14d). This results in complete suppression of the flow separation, with only small cell-like structures remaining along the separation onset, presumably due to the discrete nature of the flow interaction with the control jets. Besides this main difference in the controlled flow, the downstream flow evolution towards the AIP also changes, where the inner flow contraction relaxes relative to the base flow, bypassing a sharp interface between the inner and outer flow into the AIP. In accord with the flow reattachment, the near surface velocity deficit of the controlled flow becomes much less amplified from the adverse pressure gradients as the flow navigates the diffusing geometry, shown in figure 14c.

Figure 15 illustrates how the total pressure distribution across the AIP plane reflects these noted changes in the controlled flow. Figure 15a shows the fully resolved AIP total pressure distribution for the baseline flow, which, similar to the assertions based on experimental measurements, indicates a major deficit associated with the inner-bend side of the flow leading into the AIP, and a very thin deficit layer on the opposite side. To facilitate direct comparison with experimental 40-probe measurements, this highly-resolved numerical distribution is subsampled at the emulated 40-probe locations, and the resulting numerical distribution is shown in Figure 15b. While the subsampled field bears the main features of the full-resolved total pressure distribution, it should be noted that it also clearly attenuates the main effect and the levels of the total pressure deficit become

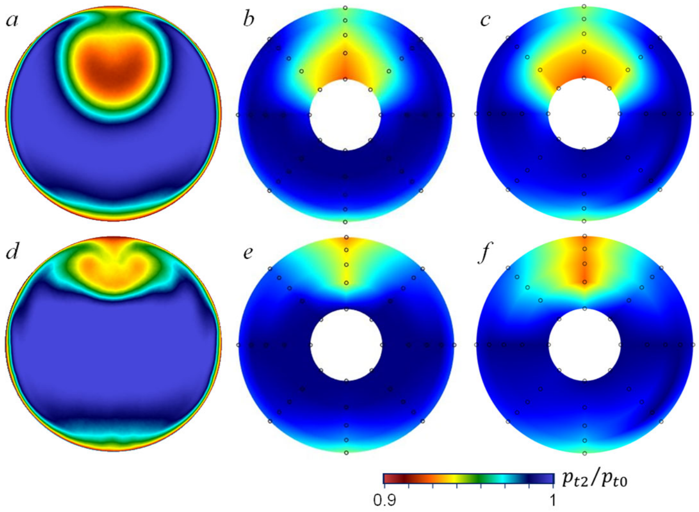

Figure 15. *Total pressure at the AIP for baseline CFD (a), 40-probe sub-sampled CFD (b), experiment (c), and the controlled flow by* $C_q = 0.01$ *for CFD (d), 40-probe sub-sampled CFD (e), and experiment (f), at* $M_{AIP} = 0.4$, *r/D = 0.2, and* $\theta = 60°$.

underestimated. Still, in a direct comparison with the experimental 40-probe measurements, shown for reference in Figure 15c, a high level of agreement is noted, with numerical results slightly underestimating the deficit levels across the AIP. Also, the high-resolution distribution of Figure 15a conveys the level of clipping of the deficit in the core flow that is not captured by the 40-probe rake. In the controlled flow, as expected from the upstream flow changes shown in Figures 14c and d, the deficit domain not only spatially compresses against the upper surface, compared to the base flow, but the total pressure deficit levels also subside. Virtually no difference is seen along the opposite AIP surface (outer bend side), since the flow control is applied only over the inner bend. When the controlled flow distribution is subsampled (Figure 15e) for direct comparison with experimental results (Figure 15f), a similar conclusion can be drawn that numerical simulation yields a close match to experimental results in terms of topology, but with even slightly higher disagreement in magnitude than in the base flow case. Overall, it is argued that numerical simulations closely predict how the flow control jets interact with the flow, which is further utilized for more insights into the controlled and uncontrolled flow evolutions.

Baseline and controlled flow evolutions across five characteristic cross sections along the flow path are considered, as previously marked in Figure 6 as planes 1, 2, 6, 8, and 12, being at the bend exit and 0.2*D*, *D*, 1.4*D*, and 2.2*D* (at the AIP) downstream from the bend exit, respectively. Figure 16a shows the evolution of the time-averaged streamwise vorticity, which was already discussed in greater detail in Figure 6 for the baseline flow. To contrast the base flow mean vortical evolution, the second column in Figure 16a shows the controlled flow vortical composition at the same six cross sections. As the flow control jets are issued upstream from the first cross section at the bend exit, the remnants of their interaction with the surface vorticity layer are seen along the upper/inner surface at both initial sections as small-scale vortical structures of predominantly opposite sign than the prevailing vorticity sense over the same surface in the baseline case. The key effect of the flow control is seen in 'arresting' the observed vorticity transport up the side and over the inner surface in the baseline flow, instead inducing a roll-up close to the upper corners in the controlled flow. While the flow control does exactly what it was designed for in these two initial planes, it is seen that with the long side expansion in plane 6, vorticity resumes its build up across the inner surface even in the controlled flow, albeit it appears delayed in its growth, when compared to the baseline flow. Further downstream progression evolves in a similar manner down to the AIP, with a main difference in the final vortical structure of the controlled flow being suppressed in size and confined closer to the surface. Not surprisingly, domains of the mean vortical signatures of the base and controlled flows

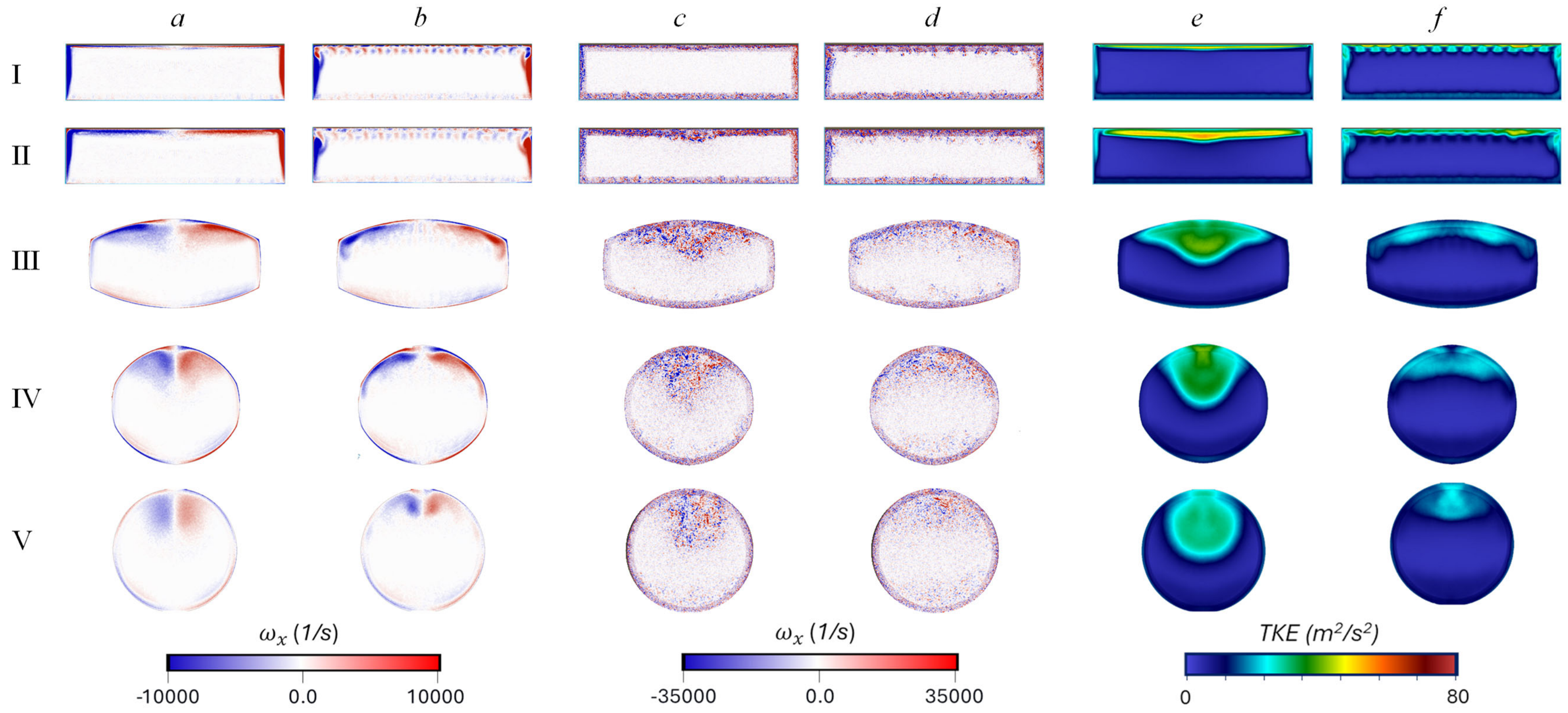

Figure 16. Simulated ***b****aseline (a,c,e) and the flow controlled by* $C_q = 0.01$ *(b,d,f) mean (a,b) and instantaneous (c,d) streamwise vorticity and turbulent kinetic energy (e,f) at cross-sectional planes of Figure 6: 1 (I), 2 (II), 6 (III), 8 (IV), and 12 (V) at* $M_{AIP} = 0.4$, $r/D = 0.2$*, and* $\theta = 60°$.

shown in Figures 15b and e.

While the time-averaged point of view (Figure 16a) points to relating pairs of counter-clockwise vorticity concentrations as coherent vortical structures, it is known that in turbulent flows a long-time average only indicates dominant flow features that do not truly exist in the flow instantaneously, leading to often simplified analysis that does not reflect a complex flow composition. This is certainly reflected in the instantaneous vorticity fields in Figure 16b, where the flow field snapshots at one instance in time that contribute to the corresponding time-averaged fields for both the controlled and baseline flows are shown in Figure 16a. Instantaneous vorticity compositions in any instance are dramatically different from those shown in Figure 16a, where small-scale strands of vorticity of typically higher magnitude become interlaced with each other over any of the domains. In the baseline flow, the existence of single sense small scale vorticity is seen only along the side walls at the first two stations. At the second station some reorganization of the vorticity strands in seen on either side of the top/inner surface, where the CW vorticity sense prevails along the left side, and the CCW sense along the right, while beginning to accumulate about the center plane. Such initial accumulation progresses both azimuthally and radially in the downstream direction, leading to the top central domain being occupied by small-scale vortical structures at the AIP. Even through this evolution, the CW and CCW prevalence is retained on either side of the vertical central plane. When the flow control is activated, clearly periodic strong vortical composition is seen at the exit plane along the inner bend. Another important difference is manifested by the top corner structures of the opposing sense of vorticity to each side wall vorticity that arguably interact with the side wall vorticity in a destructive manner. As a consequence, no clear organization of vorticity senses along the inner surface is seen at the next plane ($0.2D$ downstream from the bend), where the vorticity along the inner bend loses its periodicity but remains fairly well mixed along the full span. Only at the next station, $1D$ downstream from the bend, organization of CW and CCW vorticity is seen along the diffusing side of the inner bend, which continues to progress toward the AIP. However, vortical expansion into the core becomes significantly suppressed relative to the baseline flow.

Since it is known that the flow control elements introduce highly unsteady small-scale motions into the flow (corresponding to frequencies at about 6-7 kHz, c.f. Figure 9d), it is certainly of interest to examine how their initial interaction with the flow propagates into the AIP from the standpoint of the overall flow unsteadiness. This is examined through the turbulent kinetic energy distributions $\left(\overline{u'^2}+\overline{v'^2}+\overline{w'^2}\right)/2$ across the same five characteristic planes, for both uncontrolled and controlled flows, in Figure 16c. It is interesting that the transport of the side wall vorticity toward the inner surface in associated with rather low levels of TKE in the base flow, and that only the interactions along the inner bend surface trigger elevated levels of TKE, especially over the thickened layer in the second plane. While the peak levels diminish with further evolution into the AIP, the elevated TKE levels remain clearly associated with the extents of the vortical flow compositions at respective planes. After the flow control jets introduce periodic localized regions of high TKE at the bend exit, their interaction with the high TKE layer of the base flow actually leads to both the diminished peak TKE magnitudes across the compressed layer 0.2D downstream from the bend exit. Moreover, the TKE signatures remain separated into two lobes until the AIP, resulting not only in significantly suppressed domains of the elevated unsteadiness in the controlled flow, but the peak TKE levels becomes reduced by about 50% compared to the baseline AIP flow.

VIII. Conclusions

Flow control approaches for the mitigation of total pressure distortions that originate in the bend section of a compact aggressive diffuser are investigated in a joint experimental/numerical study using a reconfigurable diffuser testbed over a range of characteristic bend angles and radii. The present investigations assessed the base flow characteristics up to $M_{\mathrm{AIP}} = 0.6$ with specific emphasis on the sources of the total pressure distortions at the AIP to guide the development of actuation methodology for their alleviation.

It is shown that the base flow at the diffuser's AIP is characterized by a strong total pressure deficit domain along the flow path from the inner surface of the diffuser's bend section that is associated with accumulation and advection of streamwise vorticity concentrations of opposite sense along the inner surfaces of the bend about its center plane of symmetry. The formation of these streamwise vorticity concentrations is consistent with the tilting of vortex lines in the spanwise boundary layers on the bend's inner surfaces by the flow turning. These streamwise vorticity concentrations are transported by counter-rotating Dean circulations that are typically engendered by an instability of streamwise flow through a bend. The circulation-induced transported concentrations of streamwise vorticity of opposite sense are advected with the streamwise flow and roll to form a time-averaged counter-rotating streamwise vortex pair and are associated with total pressure deficit at the AIP. These findings led to a flow control approach that focused on mitigation of vorticity transport along the inner-radius surface of the diffuser's bend.

In the present investigations, flow control actuation was affected by two mirrored spanwise arrays of opposite wall jet actuators across the span of the inner surface of the bend using fluidically oscillating jets to induce motions (and vorticity concentrations) that are predominantly opposite to the motions and sense of vorticity transported by the Dean circulations. To facilitate the application of this flow control approach on all the variants of the diffuser's bend, the jet array was integrated in a sub-optimal location upstream of the bend. The magnitude of the actuation was characterized by the ratio of the mass flow rates of the actuation and through the diffuser C_q. The initial findings demonstrated the potential of this flow control approach over all variants of the diffuser's bend. The numerical simulations in the absence and presence of actuation clearly indicated that the actuation can successfully reduce the transport of vorticity concentrations induced by the bend circulations by interactions of the actuation jets with the streamwise vorticity along the bend's inner surfaces. For example, at a bend angle of 20°, the loss in total pressure at the AIP is diminished with increasing $C_{q,}$ resulting in up to a 50% decrease in the distortion measure $DPCP_{\mathrm{avg}}$ for all bend radii. That the reduction in distortion diminishes with increasing bend angle indicates that the sub-optimal position of the actuation upstream of the bend can be more effective farther downstream, which would potentially lead to improvement in its performance.

Finally, time-resolved numerical simulations of the flow demonstrated the impact of the actuation on the structure of the instantaneous flow, underscoring the differences between the instantaneous and time-averaged flow fields. While the time-averaged flow field at the AIP indicates the presence of a pair of counter-rotating vortices, the instantaneous vorticity fields consist of multiple interlaced small-scale strands of streamwise vorticity of either sense across the entire signature of the time-averaged vortices that are characteristic of the complex turbulent flow structure at the AIP.

Acknowledgment/Disclaimer

This work was sponsored by the Office of Naval Research (ONR), under grant number N000142312500. The views and conclusions contained herein are those of the authors only and should not be interpreted as representing those of ONR, the U.S. Navy, or the U.S. Government.

The authors acknowledge the computational resources provided by the Department of Defense (DoD) High Performance Computing Modernization Program, specifically the DoD ERDC and Navy DoD Supercomputing Resource Center systems.

References

[1] Connolly, B.J., Loth, E., Smith, C.F., "Unsteady flow simulations for diffusing s-ducts of circular and rectangular cross-section," *AIAA Paper 2018-2130*, 2018.

[2] Dean, W.R. "Note on the Motion of Fluid in a Curved Pipe," *Philosophical Magazine,* 4 (20), 1927, pp. 208-223.

[3] Dean, W.R. "The Streamline motion of fluid in a curved pipe," *Philosophical Magazine,* 4 (30), 1928, pp. 673-695.

[4] Dutta, P., Rajendran, N. K., Cep, R., Kumar, R., Kumar, H., & Nirsanametla, Y. (2025). "Numerical investigation of Dean vortex evolution in turbulent flow through 90° pipe bends," *Frontiers in Mechanical Engineering*, *11*, 2025.

[5] Winters, K.H., "A Bifurcation Study of Laminar Flow in a Curved Tube of Rectangular Cross-Section," *Journal of Fluid Mechanics, 180,* 1987, pp. 343-369.

[6] Sudo, K., Sumida, M., & Hibara, H., "Experimental Investigation on Turbulent Flow in a Square-Sectioned 90-degree bend," *Experiments in Fluids, 30(3),* 2001, pp. 246-252.

[7] Hall, G., Hurwitz, W., Tiebens, G., Norby, W., Singshinsuk, P., and Wilt, C., "Development of the F/A-18 E/F Air Induction System," AIAA Paper 93-2152, 1993.

[8] Anderson, B. H., and Gibb, J., "Study on Vortex Generator Flow Control for the Management of Inlet Distortion," Journal of Propulsion and Power, Vol. 9, 1993, pp. 422–430.

[9] Owens, L. R., Allan, B. G., and Gorton, S. A., "Boundary-Layer-Ingesting Inlet Flow Control," Journal of Aircraft, Vol. 45, 2008, pp. 1431–1440.

[10] Tanguy, G., MacManus, D. G., Zachos, P., Gil-Prieto, D., and Garnier, E., "Passive Flow Control Study in an S-Duct Using Stereo Particle Image Velocimetry," AIAA Journal, Vol. 55, No. 6, 2017, pp. 1862–1877.

[11] Scribben, A., Ng, W., and Burdisso, R., "Effectiveness of a Serpentine Inlet Duct Flow Control Technique at Design and Off-Design Simulated Flight Conditions," Journal of Turbomachinery, Vol. 128, No. 2, 2006, pp. 332–339.

[12] Anderson, B. H., Miller, D. N., Addington, G. A., and Agrell, J., "Optimal Micro-Jet Flow Control for Compact Air Vehicle Inlets," NASA/TM—2004-212937, 2004.

[13] Gartner, J., and Amitay, M., "Flow Control in a Diffuser at Transonic Conditions," 45th AIAA Fluid Dynamics Conference, American Institute of Aeronautics and Astronautics, 2015.

[14] Rabe, A., "Effectiveness of a serpentine inlet duct flow control scheme at design and off-design simulated flight conditions," Ph.D. thesis, ProQuest Dissertations Publishing, 2003.

[15] Harrison, N., Anderson, J., Fleming, J., and Ng, W., "Active Flow Control of a Boundary Layer-Ingesting Serpentine Inlet Diffuser," Journal of Aircraft, Vol. 50, No. 1, 2013, pp. 262–271.

[16] Garnier, E., “Flow Control by Pulsed Jet in a Curved S-Duct: A Spectral Analysis,” AIAA Journal, Vol. 53, No. 10, 2015, pp. 2813–2827.

[17] Amitay, M., Pitt, D., and Glezer, A., “Separation control in duct flows,” Journal of Aircraft, Vol. 39, No. 4, 2002, pp. 616–620.

[18] Mathis, R., Duke, D., Kitsios, V., and Soria, J., “Use of zero-net-mass-flow for separation control in diffusing S-duct,” Experimental Thermal and Fluid Science, Vol. 33, No. 1, 2008, pp. 169–172.

[19] Gissen, A. N., Vukasinovic, B., McMillan, M. L., and Glezer, A., “Distortion Management in a Boundary Layer Ingestion Inlet Diffuser Using Hybrid Flow Control,” Journal of Propulsion and Power, Vol. 30, No. 3, 2014, pp. 834–844.

[20] Burrows, T. J., Vukasinovic, B., Lakebrink, M. T., Mani, M., and Glezer, A., “Control of flow distortion in offset diffusers using trapped vorticity,” International Journal of Heat and Fluid Flow, Vol. 75, 2019, pp. 122–134.

[21] Burrows, T. J., Vukasinovic, B., Glezer, A., Lakebrink, M. T., and Mani, M., “Experimental and Numerical Investigation of Active Flow Control of a Serpentine Diffuser,” AIAA Journal, Vol. 59, 2021, pp. 607–620.

[22] Burrows, T. J., Vukasinovic, B., Glezer, A., Lakebrink, M. T., and Mani, M., “Controlled Flow in a Serpentine Diffuser with a Cowl Inlet,” Journal of Aircraft, 2024.

[23] Stratton, Z. et al. “Development of an Aggressive Offset Diffuser Testbed With Adaptive Design Characteristics”, AIAA Paper 2025-2108, 2025.

[24] Society of Automotive Engineers Inc., “Gas Turbine Engine Inlet Flow Distortion Guidelines,”, 2017. ARP 1420 Rev. C.

[25] Ham, F., Mattsson, K., and Iaccarino, G., “Accurate and Stable Finite Volume Operators for Unstructured Flow Solvers,” CTR Annual Research Briefs, 2006, pp. 243–261.

[26] Bres, G. A., Bose, S. T., Emory, M., Ham, F. E., Schmidt, O. T., Rigas, G., and Colonius, T., “Large-Eddy Simulations of Co-annular Turbulent Jet Using a Voronoi-Based Mesh Generation Framework,” AIAA Paper 2018-3302, 2017.

[27] Kawai, S., and Larsson, J., “Wall-Modeling in Large-Eddy Simulation: Length Scales, Grid Resolution, and Accuracy,” CTR Annual Research Briefs, 2010, pp. 39–46.

[28] Germano, M., Piomelli, U., Moin, P., and Cabot, W. H., “A Dynamic Subgrid-Scale Eddy Viscosity Model,” Physics of Fluids A - Fluid Dynamics, Vol. 3, 1991, pp. 1760–1765.

[29] Saric, W. S., “Görtler Vortices,” Annual Review of Fluid Mechanics, Vol.26, 1994, pp. 379–409

[30] Burrows, T.J., Gong, Z., Vukasinovic, B., and Glezer, A. “Investigation of Trapped Vorticity Concentrations Effected by Hybrid Actuation in an Offset Diffuser”, AIAA Paper 2016-0055, 2016.

[31] Lakebrink, M., Mani, M., and Winkler, C., “Numerical Investigation of Fluidic Oscillator Flow Control in an S-Duct Diffuser,” AIAA Paper 2017-1455, 2017.

[32] Bloch, G., “An Assessment of Inlet Total-Pressure Distortion Requirements for the Compressor Research Facility,” Tech. Rep., Aero Propulsion and Power Directorate W-P AFL, 1992.